



Perovskite LaFeO_3 - SrTiO_3 composite for synergistically enhanced NO_x removal under visible light excitation



Qian Zhang^{a,b}, Yu Huang^{a,b,*}, Shiqi Peng^a, Yufei Zhang^a, Zhenxing Shen^c, Jun-ji Cao^{a,b,*}, Wingkei Ho^d, Shun Cheng Lee^e, David Y.H. Pui^f

^a Key Laboratory of Aerosol Chemistry and Physics, Institute of Earth Environment, Chinese Academy of Sciences, Xi'an 710061, China

^b State Key Lab of Loess and Quaternary Geology (SKLLQG), Institute of Earth Environment, Chinese Academy of Sciences, Xi'an 710061, China

^c Department of Environmental Science and Engineering, Xi'an Jiaotong University, Xi'an 710049, China

^d Department of Science and Environmental Studies, The Hong Kong Institute of Education, Hong Kong, China

^e Department of Civil and Environmental Engineering, The Hong Kong Polytechnic University, Hung Hom, Hong Kong

^f Department of Mechanical Engineering, College of Science and Engineering, University of Minnesota, Minneapolis, MN 55455, USA

ARTICLE INFO

Article history:

Received 30 July 2016

Received in revised form 9 November 2016

Accepted 23 November 2016

Available online 24 November 2016

Keywords:

Photocatalysis

NO_x removal

Perovskite nanomaterials

SrTiO_3

LaFeO_3

ABSTRACT

Perovskite oxides (ABO_3) are widely studied as excellent sorbing and catalytic materials for NO_x abatement in automobile or stationary depollution processes, and recently they have attracted significant interest in solar conversion reactions due to the flexible composition, facile optical and electronic tuning properties. In this work, perovskite LaFeO_3 microspheres were synthesized and employed as photocatalysts to remove parts-per-billion level NO , and it is found that the photocatalytic efficiency was dramatically improved by coupling with SrTiO_3 nanocubes. The LaFeO_3 - SrTiO_3 composite with proper mass ratio (0.3–1) displayed 3.1 and 4.5 fold enhancement in NO removal rate as compared to the pristine LaFeO_3 and SrTiO_3 , respectively. Moreover, the LaFeO_3 - SrTiO_3 composite exhibited decreased NO_2 yield possibly due to the basic surface property of strontium sites. The synergistically improved activity was due to broad visible light harvest, enlarged surface area, and most importantly, the depressed surface charge recombination originating from the perfectly matched LaFeO_3 - SrTiO_3 interface and facile charge transfer along the staggered band alignment. The temperature programmed desorption (TPD) analysis revealed that the composite had efficient chemisorption for NO . Further, the electron spin resonance (ESR) combined with the radical scavenger tests and density functional theory (DFT) calculations suggested that the photocatalytic NO oxidation via superoxide radicals (O_2^-) from SrTiO_3 and direct hole (h^+) transfer from LaFeO_3 might be the predominant routes. We believe that this study provides some new insights into perovskite nanomaterials as photocatalyst for NO_x abatement under ambient conditions.

© 2016 Elsevier B.V. All rights reserved.

1. Introduction

During the past few decades, various de- NO_x techniques have been developed in order to combat with the environmental issues, such as acid rain, photochemical smog and heavy haze that are associated with nitrogen oxide (NO_x) emissions [1–3]. Among them, selective catalytic reduction and three way catalysis are demonstrated to be the most effective abatement approaches for exhaust gases from industrial power plants and mobile vehicles, respectively [4,5]. Though considerable reduction has been achieved by these techniques, with the rapid industrialization and urbanization

in developing countries, the NO_x pollutants continue to accumulate in the atmosphere, causing the frequent occurrence of heavy haze events. Recently, photocatalysis has offered an appealing way to remedy NO_x pollution at ppb-ppm level in surrounding air, due to the advantages of using abundant solar energy and ambient working conditions [6,7]. It is encouragingly to find out that many field tests demonstrated the feasibility of TiO_2 photocatalysis in eliminating NO_x and improving local air quality in urban area and tunnels, making this technology a promising approach in the future [8,9].

Despite the great promises that photocatalytic air purification exhibits, huge efforts still need to be devoted to the development of more efficient photocatalysts. Conventional studies were centered on TiO_2 due to the stable chemical properties and cheap price [10], while recently several visible light driven photocatalysts such

* Corresponding authors at: Key Laboratory of Aerosol Chemistry and Physics, Institute of Earth Environment, Chinese Academy of Sciences, Xi'an 710061, China.

E-mail addresses: huangyu@ieecas.cn (Y. Huang), cao@loess.llqg.ac.cn (J.-j. Cao).

as bismuth-based semiconductors and g - C_3N_4 are receiving more attention [11,12]. Indeed, these novel photocatalysts perform well in eliminating NO_x at ppb (parts-per-billion) level by visible light excitation. However, at low concentration range the diffusion could be very slow, making the mass transfer process become the rate limiting step which affects the overall reaction kinetics [13]. To this end, employing materials with specific chemisorption towards target pollutant is perhaps one of the strategies, because it allows the low concentration reactants to readily accumulate onto/around the surface of catalytic materials [13]. Studies have shown that perovskite oxides (ABO_3) are one of the sorbing catalytic materials, because the transition metal ions have strong ligand binding force for NO [14,15]. In this context, we focused our attention on $LaFeO_3$ perovskite due to the following two reasons. On one hand, $LaFeO_3$ is a narrow band gap semiconductor that is capable of being excited by visible light and decomposing organic molecules and water [16,17]; on the other hand, $LaFeO_3$ exhibits good chemisorption for NO irrespective of temperature (273–673 K) [18]. Wu et al. also showed that Fe^{3+} ions are highly effective adsorption sites for NO in dark conditions [19]. As a result, it is expected that $LaFeO_3$ with reinforced surface adsorption for NO (facilitating mass transfer at low pollutant concentration) and visible light response ability should display excellent photocatalytic performance. However, our previous experiments revealed that $LaFeO_3$ only had limited activity for NO removal under visible light irradiation.

By tracing back previous studies, it is believed that the photoelectric efficiency of $LaFeO_3$ is greatly affected by the poor collection of holes from the bulk to the surface, despite its suitable band gap for visible light absorption [20,21]. In other words, the short hole diffusion length L_p in $LaFeO_3$ bulk material severely restricts its photocatalytic performance, and this is mainly because the B-site cation (Fe^{3+}) determines the redox and electronic behavior. In fact, this problem can be addressed by synthesizing nanostructured or mesoporous materials with characteristic dimensions comparable to L_p , or coupling with wide band gap semiconductor to retard charge recombination [22]. Here in this work, we adopted the latter approach to construct hierarchical $LaFeO_3$ - $SrTiO_3$ composite for photocatalytic NO abatement. $SrTiO_3$ was chosen firstly because it has similar crystal structure with $LaFeO_3$; secondly, $SrTiO_3$ with surface basic sites is advantageous for NO_x adsorption and conversion [23]; and thirdly, their band edge differences might be facilitating the interfacial charge transfer. To the best of our knowledge, this is the first time to report perovskite $LaFeO_3$ - $SrTiO_3$ composites and their functional use as photocatalysts to remove NO at ppb level. The as-prepared materials are thoroughly characterized and analyzed for the promotional effect on photocatalytic reactions.

2. Experimental

2.1. Material synthesis

2.1.1. Preparation of $LaFeO_3$ microspheres

Briefly, 5 mmol $Fe(NO_3)_3 \cdot 9H_2O$ and equal molar $La(NO_3)_3 \cdot 6H_2O$ (analytical grade reagents, Sinopharm) were first dissolved in 50 mL Milli-Q water (Merck Millipore, Darmstadt, Germany), and used as precursor solution for the ultrasonic spray pyrolysis (USP) synthesis of $LaFeO_3$. The home-built USP equipment was consisted of an ultrasonic nebulizer (YUYUE 402AI, Shanghai, China), a temperature programmed tube furnace (OTF-1200X, Hefei, China), a conical filter flask and a vacuum pump which was described in our previous study [24]. In a typical synthesis, the temperature of the tube furnace was pre-set at 800 °C, then the precursor was nebulized at an ultrasound frequency of 1.7 MHz ± 10%, with the atomized droplets flowing through the tube furnace in air under the pump

extraction force, and finally $LaFeO_3$ samples (denoted as LFO) were collected in the filter flask. The as-prepared samples were washed thoroughly with absolute ethanol and deionized water for several times, before centrifuged and dried at 80 °C overnight.

2.1.2. Preparation of $LaFeO_3$ - $SrTiO_3$ composites

The $LaFeO_3$ - $SrTiO_3$ composite was prepared by adding a certain amount of $LaFeO_3$ in strontium and titanium precursor solution for solvothermal treatment. Specifically, 1 mmol $Sr(NO_3)_2$ was first dissolved in 5 mL deionized water, and slowly mixed with titanium tetraisopropoxide (TTIP)/absolute ethanol solution, then 7 mmol $NaOH$ was added in the above solution and stirred completely for 1 h [25]. To the $SrTiO_3$ precursor solution LFO powder with the mass ratio of 0.3:1 was added and ultrasonically dispersed, before transferring to a 50 mL Teflon-lined stainless steel autoclave and kept at 160 °C for 24 h. Similarly, the as-prepared composite was washed thoroughly with absolute ethanol and deionized water, centrifuged and dried at 80 °C overnight. The $LaFeO_3$ - $SrTiO_3$ composites with different mass ratios at 0.15:1, 0.3:1 and 1:1 were fabricated and denoted as LFO-STO_{0.15}, LFO-STO_{0.3} and LFO-STO₁, respectively. For comparison, pure $SrTiO_3$ (denoted as STO) was also prepared following the above procedure without adding LFO powder.

2.2. Material characterization

The crystal structure of the samples were analyzed by the PANalytical X'pert Pro powder X-ray diffractometer at a scanning rate of 0.017° min⁻¹ ranging from 20° to 80° (PANalytical Corp., the Netherlands). X-ray photoelectron spectroscopy (XPS) were collected on ThermoFisher Scientific photoelectron spectrometer (Escalab 250Xi), with the sample being illuminated by monochromatic Al $K\alpha$ X-ray source ($h\nu = 1486.71$ eV). All binding energies were calibrated by C 1s at 284.8 eV as a reference. The morphology of the samples was characterized by scanning electron microscope (SEM) 6700F instrument (JEOL Corp., Japan), with energy dispersive X-ray spectroscopy (EDX) mapping recorded at the same time. For transmission electron microscopy (TEM) and selected area electron diffraction (SAED) characterization, samples were ultrasonically dispersed in absolute ethanol and dropped onto the carbon coated copper grids, and then imaged on the JEOL 2010 instrument at accelerating voltage of 200 kV (JEOL Corp., Japan). Temperature programmed desorption (TPD) was carried out on a chemisorption analyzer (BJbuilder, PCA 1200, China), with powder samples of 50 mg supported on a frit in the continuous flow quartz reactor. Before adsorption of the target gas, the sample was pretreated by N_2 at 300 °C for 30 min at heating rate of 10 °C min⁻¹, to remove any surface contaminants. After the pretreatment the sample was cooled to room temperature, and the adsorbing gas of NO at concentration of 100 ppm was flowed over the sample for 30 min. Once equilibrated, the sample was heated at 10 °C min⁻¹ to 850 °C in He atmosphere to allow desorption of NO . The optical property of the samples were investigated by measuring the UV-vis diffuse reflectance spectroscopy (UV-vis DRS) on the Agilent Cary 100 instrument (Agilent Corp., the United States) equipped with an integrating sphere, using $BaSO_4$ reflection as a reference. The band gap of semiconductor was further obtained by converting the reflection into absorbance through Kubelka-Munk function. The surface photovoltage spectroscopy (SPS) was conducted on a home-made detection system similar to the previous references [26], which includes a source of monochromatic light provided by a 500 W xenon lamp and a double-prism monochromator, a lock-in amplifier (SR830-DSP) with a light chopper (SR540), a photovoltaic cell and a computer. The construction of photovoltaic cell was made by pressing the powder sample into two indium tin oxide (ITO) electrodes to form a sandwich-like structure. The SPS signal was recorded in the wavelength range of 300–1000 nm. In

order to probe the formation of superoxide $\bullet\text{O}_2^-$ and hydroxyl $\bullet\text{OH}$ radicals, electron spin resonance (ESR) measurements were conducted on a Bruker ER200-SRC instrument (Bruker Corp., Germany) at room temperature. DMPO (5,5-dimethyl-L-pyrroline N-oxide) was used as the spin trapping agent, with deionized water and methanol as solvents, respectively, to detect the generation of radical adducts DMPO- $\bullet\text{OH}$ and DMPO- $\bullet\text{O}_2^-$. The LED light at wavelength of 420 nm was used as excitation source during ESR studies. The Brunauer–Emmett–Teller (BET) surface area was determined by measuring the nitrogen adsorption–desorption isotherms at 77 K using a Micrometrics ASAP2020 equipment.

2.3. (Photo)electrochemical studies

To conduct the photoelectrochemistry measurements, the photoelectrodes were fabricated according to a previous report [20]. Typically, ethyl cellulose and terpineol were first added into SrTiO_3 -ethanol solution to obtain a homogeneous suspension by ultrasound dispersion. Then, the STO film was deposited onto the fluorine doped tin oxide (FTO) glass by dip coating in the above suspension for several times and dried at room temperature. The final composition of STO film was 0.18 wt% STO, 0.09 wt% ethyl cellulose, and 0.73 wt% terpineol. Afterwards, the STO electrodes were annealed in air at 500 °C for 30 min to remove the additives and ensure the close electric contact with the substrate. LaFeO_3 and $\text{LaFeO}_3\text{-SrTiO}_3$ composite photoelectrodes were fabricated following the same procedure with the same coating cycles, in order to make sure that the amount of deposited photocatalyst is identical.

Photoelectrochemical and electrochemical experiments were all conducted on a Princeton Parstat4000 potentiostat. Three-electrode configuration was employed in these experiments, with platinum foil and Ag/AgCl (3 M KCl) electrodes as secondary and reference electrodes, respectively. For transient photocurrent measurement, a single compartment cell with a quartz window was used, and the photoelectrodes with geometric surface area of 1 cm^2 were exposed to periodic front-side illumination (provided by a 420 nm LED) under external potential of 0.2 V. The Na_2SO_3 aqueous solution (pH 12) at concentration of 0.1 M was served as the electrolyte. For Mott–Schottky (M–S) measurement, the working electrode was immersed in 0.1 M Na_2SO_4 aqueous solution (pH 12), and subjected to 5 mV perturbation bias at fixed frequency of 1000 Hz from –0.6 to 0.8 V vs. Ag/AgCl.

2.4. Photocatalytic activity evaluation

The evaluation of photocatalytic performance of as-prepared samples was conducted in a continuous-flow chamber, with shape and dimension (10 cm high *30 cm long *15 cm wide) similar to the photoreactor described in the ISO 22197-1 standard [25]. Prior to irradiation, 0.1 g photocatalyst was spread on a glass holder and placed inside of the reactor, and a mixture of NO/air flow at a concentration of 400 ppb was accessed into the chamber. The mixture was produced by diluting NO feed stream (100 ppm) with zero air in the gas dilution calibrator (Sabio 4010, the United States). After achieving the adsorption–desorption equilibrium between photocatalyst and NO by introducing the gas mixture into the system (at volume rate of 3 L min^{-1}) for at least 30 min, the 300 W electric input Xenon lamp (Perfectlight, microsolar300, Beijing) was turned on and the concentration of NO and NO_2 was continuously monitored. Visible light (≥ 420 nm) was obtained by passing through the 420 nm cutoff filter and the optical power density reaching the sample surface was calibrated to be 28.93 mW/cm^2 (Thorlabs PM100D optical power meter). The whole measurement was conducted at ambient conditions and relative humidity of $30 \pm 5\%$. The removal ratio of NO at any given time was denoted as C/C_0 , where C is the NO concentration at any given time, ppb; and C_0 is the initial

concentration of NO, ppb. NO_2 concentration was simultaneously recorded during the process, and the yield was calculated according to the following equation:

$$\text{NO}_2 \text{ yield} (\%) = \frac{C_{\text{NO}_2}}{C_0 - C} \times 100$$

Where C_{NO_2} represents the production of NO_2 , ppb; C_0 is the initial concentration of NO, ppb; and C is the final concentration of NO, ppb. After the reaction was finished, the products remaining on the photocatalyst surface were extracted by deionized water and measured using a Dionex-600 Ion Chromatograph (Dionex Inc., Sunnyvale, CA, USA) equipped with an IonPac AS14A column.

2.5. DFT calculations

All of the calculations were performed with the density functional theory (DFT) provided by the program CASTEP package [27], which employs the plane-wave basis sets to treat valence electrons and norm-conserving pseudo-potentials to approximate the potential field. Spin-polarized calculations were employed using the generalized gradient approximation (GGA) [28] with the Perdew–Burke–Ernzerhof (PBE) [29] + U [30] to describe the exchange–correlation energy and electron interactions. A plane-wave cutoff of 420 eV was used for all calculations. The energy and residual force convergence criterion were set to 5.0e–7 eV/atom and 0.05 eV/Å for geometry optimization, respectively. We used a $4 \times 4 \times 2$ Monkhorst–pack k -point mesh for geometry optimization of the bulk LFO and STO, and a $4 \times 4 \times 2$ mesh to calculate their density of states (DOS). Also, we used a $4 \times 1 \times 1$ Monkhorst–pack k -point mesh for geometry optimization of the LFO–STO composites, and a $6 \times 2 \times 1$ mesh to calculate its DOS. Charge transfer was calculated by electron density difference (EDD) on the basis of the Miliken Population Analysis (MPA) [31].

3. Results and discussion

3.1. Material characterization

3.1.1. Phase structure, chemical compositions and optical properties

Fig. 1a depicts the powder X-ray diffraction patterns of the as-prepared samples. For STO, the diffraction peak sat 32.4°, 39.9°, 46.5°, 57.8° and 67.6° are corresponding to the 110, 111, 200, 211, 220 and 310 planes of cubic strontium titanate phase (JCPDS file No. 073-0661, space group $Pm\bar{3}m$, lattice constant $a = 3.905 \text{ \AA}$) [32]. As for the pure LaFeO_3 , all diffraction peaks are perfectly matched to the cubic perovskite phase according to the JCPDS file No. 75-0541 (space group $Pm\bar{3}m$, lattice constant $a = 3.890 \text{ \AA}$) [33,34]. Due to the high similarity of the two sets of diffraction peaks, the XRD pattern of LFO– $\text{STO}_{0.3}$ composite shows overlapping diffraction peaks with LFO and STO, without producing any additional peaks. No post-heat treatment at high temperature was performed so it is assumed that little or no reaction/diffusion process occurred at the two solid interfaces, excluding the possible production of solid solution [35]. When the SrTiO_3 nanocubes grow perpendicularly to the surface of LFO sphere, the interfacial lattice mismatch is only 0.3% ($(3.905 - 3.890)/3.890 \times 100\%$). Therefore, the tiny lattice mismatch avoids the defective and abrupt interface to be formed, which is potentially benefit for the interfacial transfer of charge carriers [36]. According to the Bragg equation, STO and LFO have the similar d -spacing value of 0.27 nm as estimated from the strongest 110 plane. In addition, the crystallite size is estimated to be 33.8 and 31.1 nm for STO and LFO, respectively, using the Debye–Schererrer equation [37].

The surface composition and chemical states of the pristine LFO and LFO– $\text{STO}_{0.3}$ composite were examined by X-ray photoelectron

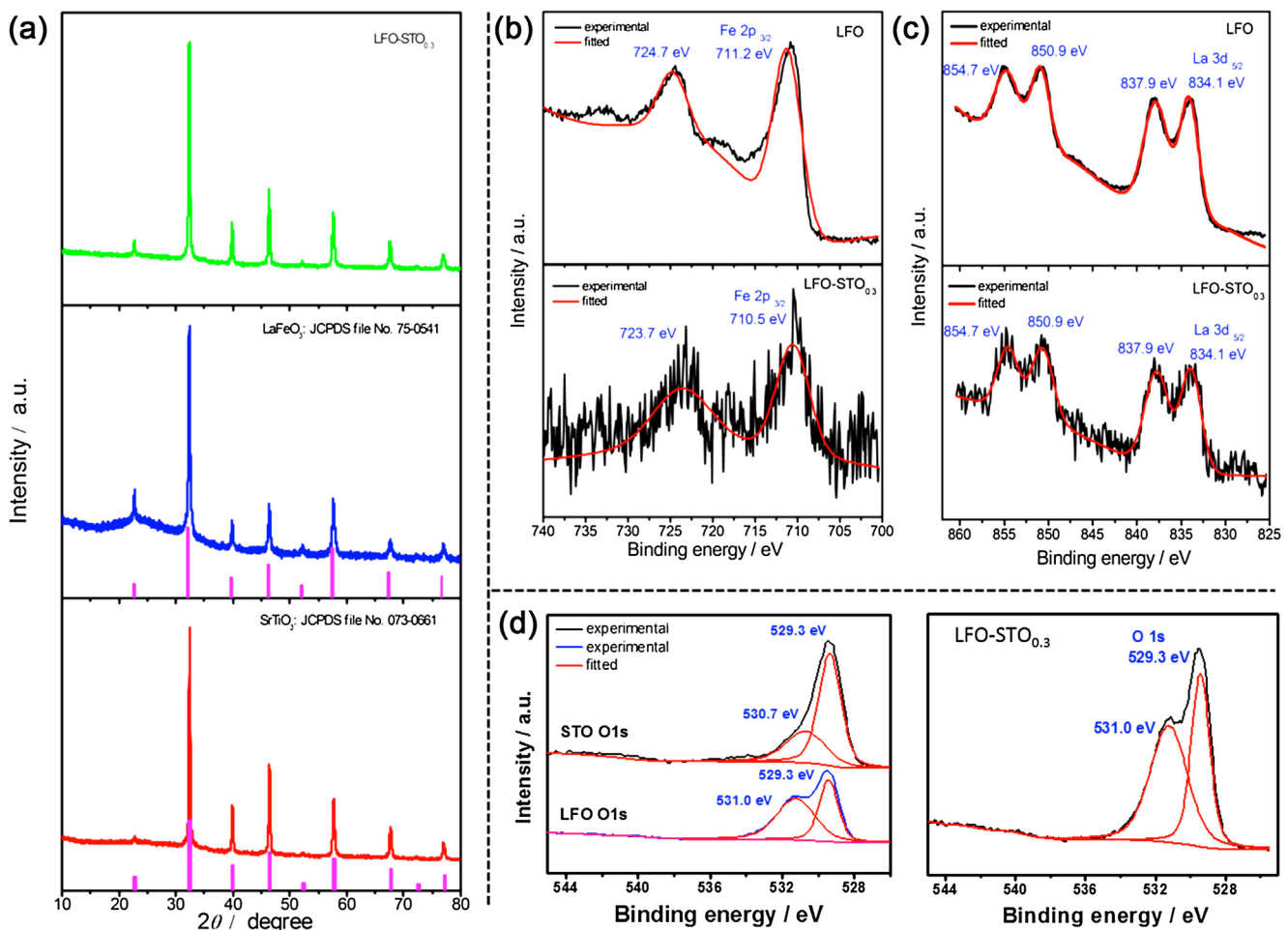


Fig. 1. (a) Powder XRD patterns of the as-prepared pristine STO, LFO and LFO-STO_{0.3} composite photocatalysts; (b) High resolution Fe 2p orbital XPS spectra of the LFO-STO_{0.3} composite and LFO; (c) La 3d orbital spectra of the LFO-STO_{0.3} composite and LFO; (d) O 1s orbital spectra of the pristine STO, LFO and LFO-STO_{0.3} composite.

spectroscopy. The survey spectrum of LFO-STO_{0.3} composite (Fig. S1) detects the presence of La, Fe, Sr, Ti and O elements at the surface, indicating the incomplete coverage of LaFeO₃ with SrTiO₃. Fig. 1b shows that the Fe 2p peaks of the LFO-STO_{0.3} composite slightly shifted towards lower binding energies compared to that of the bare LFO [17], while the La 3d peaks had no obvious change (Fig. 1c) [38]. This shift in Fe 2p orbital could be arise from the interaction with less electronegative species, and presumably the LaFeO₃ was connected with SrTiO₃ through Fe—O—Ti bonds. Fig. 1d presents the O 1s core level spectra of the pristine STO, LFO and LFO-STO_{0.3} composite which can be deconvoluted into two peaks by the Gaussian rule. The peak located at 529.3 eV is assigned to lattice oxygen species (O_{lattice}), and the other one is usually attributed to chemically adsorbed oxygen species of water (O_{ad}) [39]. As further observed, the O 1s binding energy of LFO remains unchanged in comparison with that of LFO-STO_{0.3} composite, while the O_{ad} binding energy of STO shows a small chemical shift towards higher value. This change is probably originated from the chemical bonds formed between Fe and surface oxygen species of STO, further confirming the linkage of LaFeO₃ and SrTiO₃ through Fe—O—Ti bonds.

As the optical property is a crucial factor influencing the photocatalytic activity, the UV-vis diffuse reflectance spectra of the samples were recorded shown in Fig. S2. The pristine LaFeO₃ presents the broad absorption band in the UV-vis light range due to the small band gap energy (~2.2 eV). In comparison, the LFO-STO_{0.3} composite still maintains excellent visible light harvest, suggesting

that the coupling with wide band gap SrTiO₃ did not severely block the visible light absorption.

3.1.2. Morphology characterization by electron microscopy

The SEM images of as-prepared samples were recorded and contrasted in Fig. 2. Smooth and spherical LFO particles with diameter ranging from 0.1–1 μm were produced by ultrasonic spray pyrolysis (Fig. 2a), which is the typical feature of the products fabricated by this method [40,41]. After the solvothermal treatment, LFO spheres were coated with small STO nanoparticles with average size around 30 nm (Fig. 2b–c). In order to examine the elemental distribution of the composite material, EDX mapping was recorded and shown in Fig. 2. The result suggests that La (blue), Fe (black) and O (red) elements are distributed uniformly in a single LFO sphere, and the even dispersion of Sr (green) and Ti (purple) elements is an indicative of well distribution of STO on LFO surface.

To further understand the crystal structural characteristics of pristine samples and the LFO-STO_{0.3} composite, the TEM and SAED characterizations were carried out. Fig. 3a presents the bright field image of a single LaFeO₃ sphere, from which one can notice that the sphere is actually comprised of small particle aggregates. This is likely to form because many small-sized droplets inside large droplets tend to agglomerate and crystallize during fast heating and evaporation in the furnace. At high magnification it reveals that these particles have lattice spacing of 0.27 nm, which is in accordance with the (110) plane *d*-spacing value of LFO (Fig. 3b).

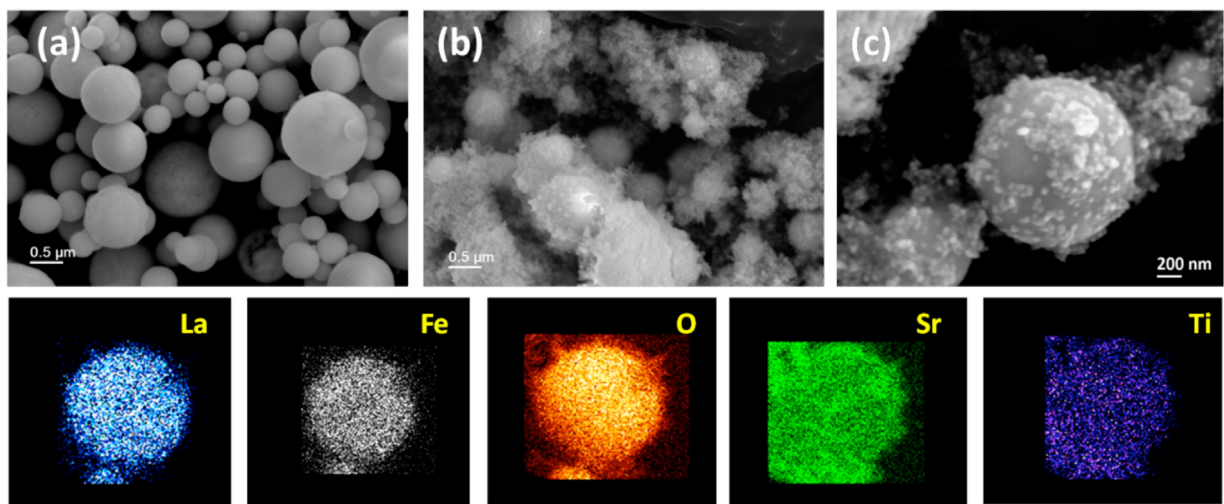


Fig. 2. (a) Representative SEM images of the as-prepared LFO microspheres; (b, c) Representative SEM images of the as-prepared LFO-STO_{0.3} composite at low and high magnifications; and EDX mapping images corresponding to (c).

The inset SAED pattern is indexed to a cubic perovskite LaFeO₃ single crystal, with electron beam vertical to the (111) crystal plane so that hexagonal diffraction spots are observed. The relative angle of adjacent diffraction spots around 60° is consistent with the characteristic angle of 59.4° between the two adjacent planes in Fig. 3b, which confirms the consistency of these images. Fig. 3c shows the solvothermally produced SrTiO₃ with cubic shape and typical size of 35 ± 2 nm in consistent with SEM results. The high resolution TEM image (Fig. 3d) reveals the lattice spacing of 0.27 nm corresponding to the (110) plane of STO, and this result is further confirmed by the SAED pattern which presents a set of tetragonal diffraction points resulted from the projection of electron beam vertical to the (001) plane. Fig. 3e illustrates that small SrTiO₃ nanocubes are formed and attached to the surface of LaFeO₃ spheres after the solvothermal reaction. By taking the high resolution TEM image (Fig. 3f) from the edge of the composite nanomaterial, it is observed that the lattice spacing of 0.27 nm and plane interfacial angle of 63.4° are indexed to LaFeO₃, and the same lattice spacing of 0.27 nm below LaFeO₃ phase is corresponded to SrTiO₃. The TEM images provide visual evidence and further confirm that LFO-STO heterojunction with intimate contact was formed. Combined with XRD results, it is expected that such well-matched interface would be advantageous for efficient interfacial charge transfer.

3.2. Photocatalytic performances on NO removal

Fig. 4a shows the photocatalytic activities of the pristine LFO, STO and LFO-STO_{0.3} composite in degrading NO at flow conditions under visible light irradiation ($\lambda \geq 420$ nm). Reactions were started in 30 min after the adsorption/desorption equilibrium was achieved between NO and the photocatalyst in the dark. As observed, no nitric oxide can be converted with photocatalysts in the dark, suggesting the importance of light (see the “Blank” curve in Fig. 4a). When light was turned on, NO shows enhanced degradation within 5 min over the LFO-STO_{0.3} composite comparing to the pristine STO and LFO. At the end of the reaction, over 40% of NO was removed by the LFO-STO_{0.3} composite, while only 10% of NO was eliminated by the pristine samples. The kinetics of photocatalytic NO removal was evaluated, assuming that NO degradation at flow conditions follows the Langmuir-Hinshelwood model in the initial time period [42]. The linear plot between $\ln(C_0/C)$ and irradiation time (t) indicates that photocatalytic NO degradation over the prepared samples follows quasi-first order kinetics, and

among these samples the LFO-STO_{0.3} composite shows the highest rate constant (0.072 min^{-1}), which is 3.1 and 4.5 times faster than LFO (0.023 min^{-1}) and STO (0.016 min^{-1}). In fact, the influence of surface area on photocatalytic activity after depositing with SrTiO₃ was also considered (Table S1). The BET results reveal that the surface area of LFO-STO_{0.3} composite was doubled comparing to the bare LFO, but this enlargement is not the only reason accounting for the improved photocatalytic activity. For comparison, we also prepared the mechanically mixed LFO-STO sample (at the same mass ratio of 0.3:1), and found out that it showed limited photocatalytic capacity to remove NO (Fig. S3). For the moment, we conclude that the improved photocatalytic performance of the LFO-STO_{0.3} composite is probably originated from the broad visible light absorption, enlarged surface area and the hetero-interface formation. The photocatalytic performance of the other two composite samples was also assessed (Fig. S3). It seems that the change of composition does not have obvious impact on the NO removal efficiency. We thought that this can be ascribed to the heterojunction interface is not finely tuned due to the large size distinction between STO and LFO. The STO nanocubes would tend to aggregate as the composition increased, instead of dispersing evenly on the LFO surface. In the following part we will focus on the optimal LFO-STO_{0.3} composite and explore the mechanism of activity enhancement.

In addition, the intermediate product NO₂ in the outlet gas was simultaneously monitored in the experiment. The NO conversion rate (C/C_0) and NO₂ yield ($C_{\text{NO}_2}/(C_0 - C)$) over the samples are contrasted in Fig. 4b. Apparently the LFO-STO_{0.3} composite shows superior performance in NO conversion with lower NO₂ yield (11.3%) than pure LFO (46.7%) and STO (20.3%). Here we suppose that the high yield of NO₂ generated from LFO under illumination is due to the poor charge separation and insufficient amount of strong oxidative species. While coupling with SrTiO₃ could potentially reduce the chance of charge recombination, increase the surface area and amount of oxidative species, and finally leads to a more complete oxidation of NO. The presence of basic sites Sr²⁺ could also be a reason for decreased NO₂ yield, which was demonstrated in our previous study. Moreover, the stability of the LFO-STO_{0.3} composite in removing NO under identical conditions was evaluated by the cyclic degradation experiments presented in Fig. 4c. The efficiency decreases by 20% in 5 repeated runs, indicating that the material is relatively unstable for a long time usage. However, the composite photocatalyst restores its activity after simply washed by deionized water, and this is due to the removal of NO oxidation

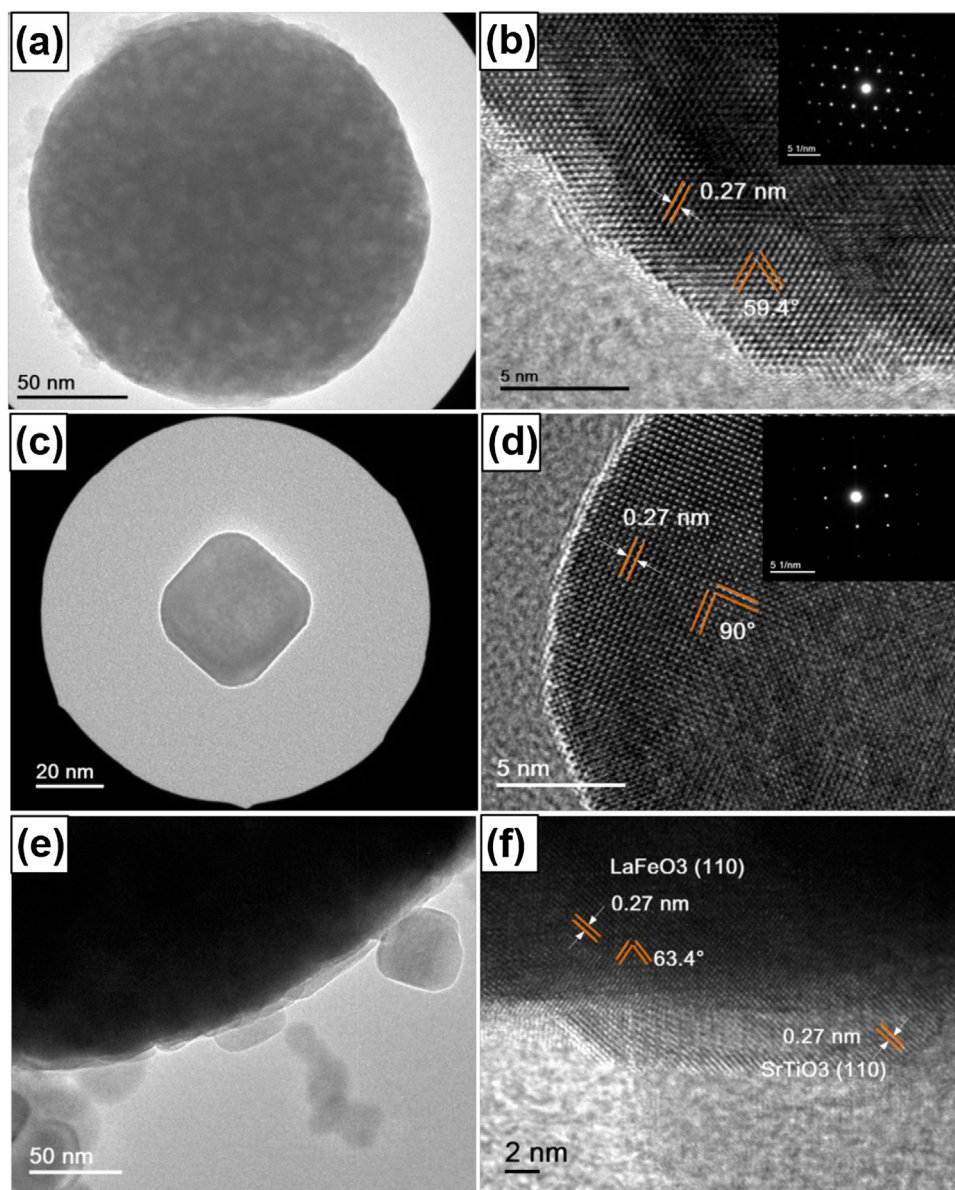


Fig. 3. (a, b) Representative TEM and HR-TEM images of the as-prepared pristine LaFeO₃ with SAED patterns; (c, d) Representative TEM and HR-TEM images of the as-prepared pristine SrTiO₃ with SAED patterns; (e, f) Representative TEM and HR-TEM images of the as-prepared LFO-STO_{0.3} composite interface.

product NO₃[–] from the catalyst surface. Presumably fabricating mesoporous nanomaterials with large surface area would alleviate the quick deactivation phenomenon.

3.3. Mechanism on photocatalytic activity enhancement and NO degradation

3.3.1. Charge transfer mechanism by (photo)electrochemical studies and SPS analysis

As speculated before, the improved photocatalytic activity was mainly originated from the effect of heterojunction of the LFO-STO_{0.3} composite, so (photo)electrochemical studies were carried out to probe the charge separation across the interface. Fig. 5a records the transient photocurrent responses of the STO, LFO and LFO-STO_{0.3} composite photoanodes in a photoelectrochemical cell under the potential of 0.2 V vs. Ag/AgCl, with front-side irradiation ($\lambda = 420$ nm) and 0.1 M Na₂SO₃ as electrolyte medium. In theory, sulfite ions (SO₃^{2–}) can effectively capture the photo-induced holes, and the magnitude of photocurrent

density actually reflects the concentration of charge carriers reaching the electrode/electrolyte interface for reactions [43,44]. Generally observed in this figure, the photocurrent displays rapid increase and drop upon light changing, suggesting that the photoanodes have good photoelectric response ability. The photocurrent density follows the order of LFO-STO_{0.3} composite > STO > LFO, which indicates that the LFO-STO_{0.3} composite greatly promotes the separation of photo-induced electron-hole pairs, and leads to the improved catalytic reaction rates. In addition, the higher photocurrent density generated from STO than LFO illustrates the better charge separation within the STO bulk material, even though it only absorbs tiny fraction of visible light. Therefore, it is concluded that the poor photocatalytic activity of LFO is primarily due to its inferior electric properties, while coupling with STO to form heterojunction interface with built-in electric field can promote interfacial charge separation and significantly improve photocatalytic activity.

The Mott-Schottky measurements of the pristine LFO and STO electrodes were conducted to further estimate their band edge

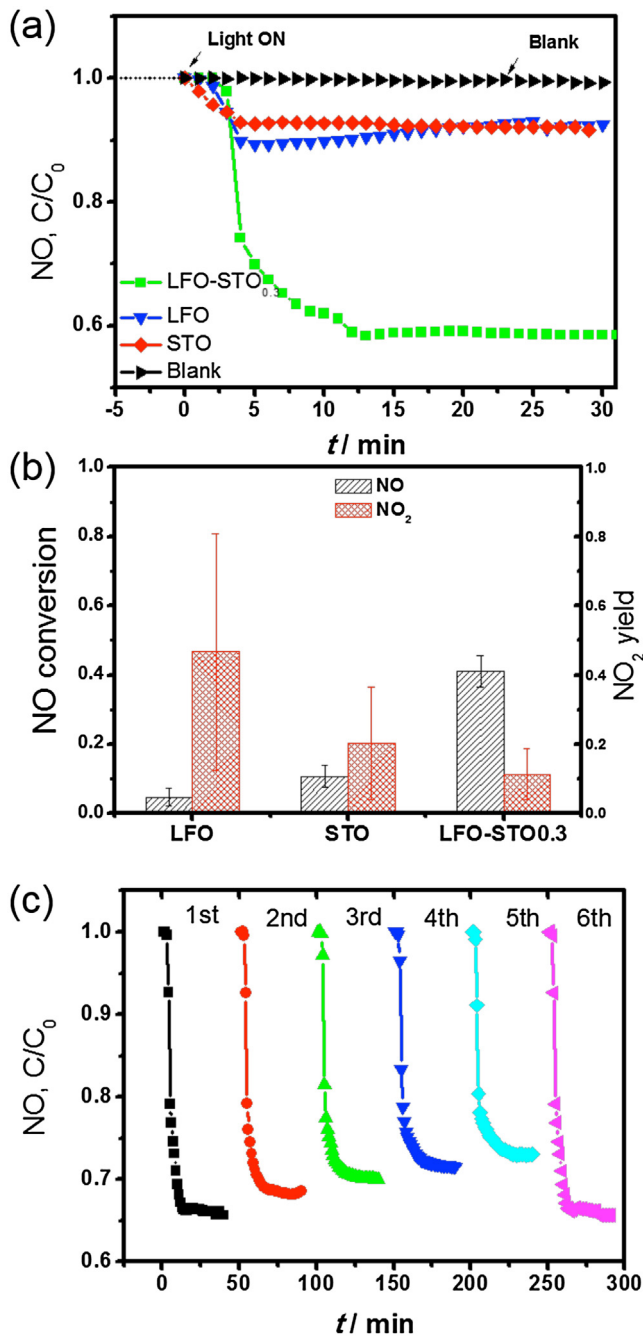


Fig. 4. (a) NO photocatalytic removal profile C/C_0 as a function of time over the as-prepared LFO, STO and LFO-STO_{0.3} composite; (b) Comparison of the NO conversion rate (C/C_0) and NO_2 yield over the as-prepared LFO, STO and LFO-STO_{0.3} composite; (c) Cyclic NO degradation tests with the LFO-STO_{0.3} composite under visible light irradiation ($\lambda \geq 420 \text{ nm}$).

positions and configuration, so that the charge transfer direction can be determined. The M-S plots are presented in Fig. 5b, from which we can observe that the capacitance decreases with the increase of applied potential for both LaFeO_3 and SrTiO_3 , which is in accordance with the behavior of n -type semiconductor [45]. From the M-S curves, the flat band potential and charge carrier density of semiconductors can be obtained according to the following equation [46]:

$$\frac{1}{C^2} = \frac{1}{C_H^2} + \frac{2}{\varepsilon_r \varepsilon_0 q A^2 N_D} (U - U_{fb} - \frac{kT}{q})$$

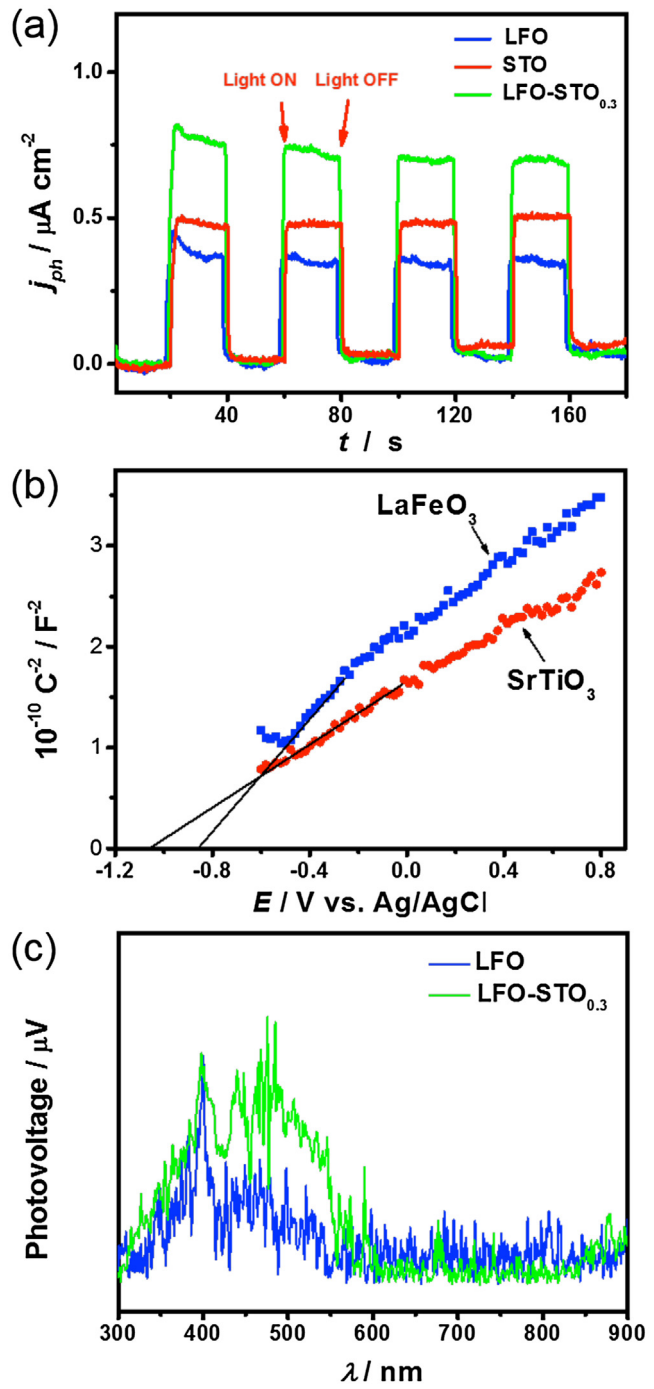


Fig. 5. (a) Transient photocurrent responses of the as-prepared STO, LFO and LFO-STO_{0.3} composite photoanodes, recorded at potential of 0.2 V vs. Ag/AgCl in 0.1 M Na_2SO_4 aqueous solution under visible light irradiation ($\lambda = 420 \text{ nm}$); (b) Mott-Schottky plots of the LaFeO_3 and SrTiO_3 electrodes in 0.1 M Na_2SO_4 at the frequency of 1000 Hz and DC potential range of -0.6 to +0.8 V vs. Ag/AgCl, perturbation bias: 5 mV; (c) SPS spectra of the pristine LaFeO_3 and LFO-STO_{0.3} composite.

where C is the space charge layer capacitance, C_H is the Helmholtz double layer capacitance, ε_r is the dielectric constant of the semiconductor, ε_0 is the permittivity of free space, q is electronic charge, A is electrode surface area, N_D is the doping density, U is the applied potential, U_{fb} is the flat band potential, k is the Boltzmann's constant and T is the absolute temperature. Here we calculated the flat band potential by intercepting the first linear slope (from flat band potential to $\sim 0.0 \text{ V}$ vs. Ag/AgCl) with the x axis, which is -0.85 V and -1.05 V vs. Ag/AgCl for LFO and STO, respectively. Through

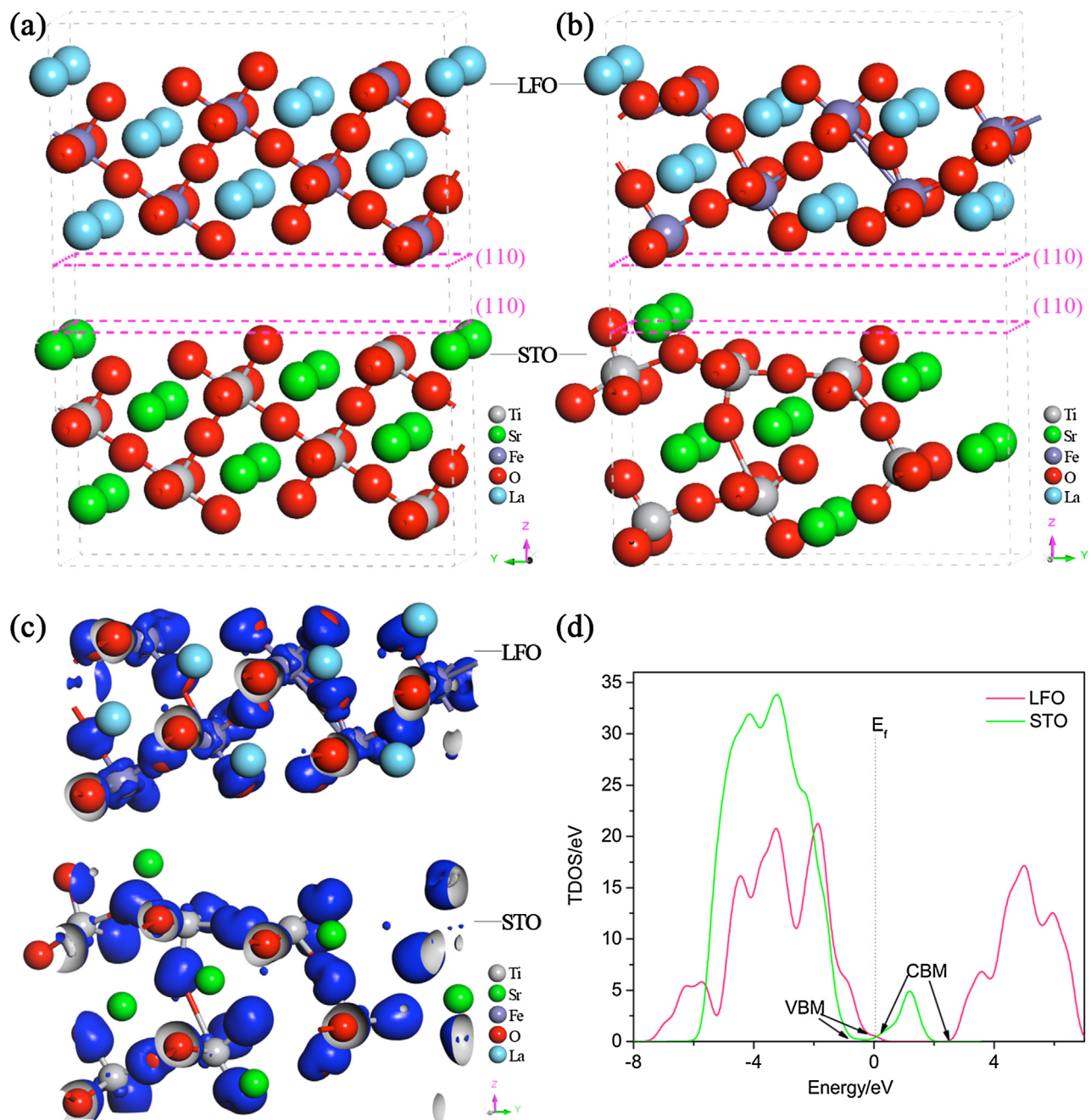
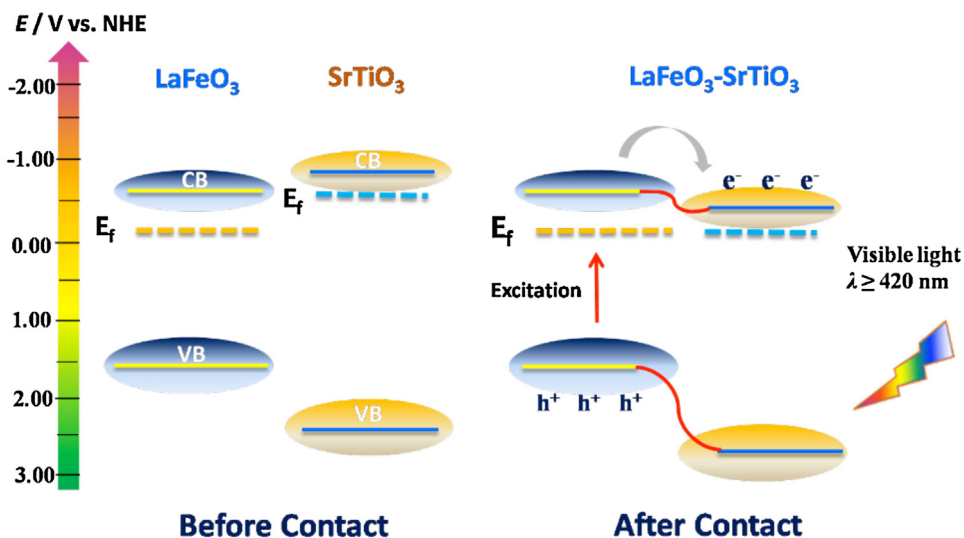


Fig. 6. The crystal models (a) before and (b) after geometry optimization, (c) the calculated electron density difference (EDD) diagram (notice: blue area represents the increase of electron density) and (d) total density of states (TDOS) of the LFO-STO composite. (For interpretation of the references to colour in this figure legend, the reader is referred to the web version of this article.)

the Nernst equation [47]: $E_{\text{NHE}} = E_{\text{Ag}/\text{AgCl}} + 0.0591 \times \text{pH} + 0.197 \text{ V}$, the experimentally obtained potential vs. Ag/AgCl was converted to the normal hydrogen electrode (NHE) scale. That makes the flat band potentials of LFO and STO to be -0.65 V and -0.85 V vs. NHE, respectively. Presumably, the flat band potential of n-type semiconductor roughly matches with the conduction band edge [48], so combined with the band gap obtained from the UV-vis DRS result, the relative position of their band edges (CB/VB) are determined to be $-0.65 \text{ V}/1.55 \text{ V}$ and $-0.85 \text{ V}/2.4 \text{ V}$ vs. NHE for LaFeO_3 and SrTiO_3 , respectively.

It seems that with this band edge configuration the electron transfer from LFO to STO under visible light is impossible, so we employed the surface photovoltage spectroscopy (SPS) to investi-

gate the photophysics of excited carrier states, which is reflected by the light-induced changes of surface voltage [26,49,50]. Fig. 5c shows that in the visible light region ($\sim 500 \text{ nm}$) the SPS signal of LFO- $\text{STO}_{0.3}$ composite is increased compared to that of LFO, which is attributed to the transfer of photo-generated electrons from LFO to STO. Similar results were found in the surface photovoltage spectroscopy of LaFeO_3 - TiO_2 composite materials upon visible light illumination [50]. It is assumed that the facile capture of electrons by SrTiO_3 adsorbed O_2 (more negative CB potential than O_2/O_2^- redox potential) dynamically promotes the charge transfer from LFO to STO. Wang et al. also demonstrated the charge transfer mechanism of Pt/Ru-doped SrTiO_3 photocatalyst under irradiation by such technique [51]. So this result further confirms the role of STO as electron acceptor to suppress charge recombination.



Scheme 1. Schematic band alignment and mechanism of charge transfer at the interface of the LaFeO₃-SrTiO₃ composite under visible light irradiation ($\lambda \geq 420$ nm).

To further elucidate the origin of the charge carriers transfer at the LFO-STO composite interfaces, DFT calculations were performed by calculating the electron density difference (EDD) and total density of states (TDOS) of the LFO-STO composite.

First, the crystal models of the LFO-STO composite with the interfaces composed of LFO (110) and STO (110) lattice planes are constructed as shown in Fig. 6a. After geometry optimization, the LFO-STO model is shown in Fig. 6b, and its crystal structure displays that the deformation degree of STO (110) lattice plane at the interface is much larger than that of LFO (110). This indicates that the variety of band structure of the STO in the LFO-STO composite would be much larger, which may affect the charge carriers transfer at the interfaces. The EDD and TDOS of the LFO-STO composite shown in Fig. 6c and d and its band alignment from the TDOS demonstrate this view. The TDOS results show that conduction band minimum (CBM) level of the STO is approximately 0 eV lower than 2.5 eV of the LFO, and valence band maximum (VBM) level of the STO is approximately -1.0 eV which is also lower than that of the LFO, which reveals that the LFO-STO composite is an emerging type II, realizing the electron-hole separation in such hetero-interfaces. Besides, The EDD results in Fig. 6c demonstrate that the charge transfer from LFO to STO is about 1.05 electrons at the interface. In addition, according to Fig. 6d, the two phases acquire an equalized Fermi (E_f) level after contact of the LFO and STO. Herein, the huge change of band structure of the STO after contact promotes the electron transfer from the LFO to STO.

On the basis of the above experimental and DFT calculations results, we propose the charge transfer mechanism under visible light according to the band configuration shown in Scheme 1. Before contact, electrons cannot be transferred from the conduction band of LFO to STO due to the energy barrier restrictions. When they are attached to each other by forming heterojunction, the different Fermi level of LFO and STO will reach equilibrium. Under such circumstances, the photo-excited electrons from LFO are driven to the conduction band of STO, whereas the photo-generated holes are left on the valence band and prohibited from transferring to STO, thereby realizing efficient charge separation and enhanced photocurrent.

3.3.2. NO adsorption-desorption behavior by TPD analysis

As generally described in literatures, perovskite-type catalysts with the ABO₃ structure have excellent adsorption and oxidation ability for NO_x due to their redox properties, but the adsorption

behavior is also sensitive to the chemical compositions [52]. Here we employed the temperature programmed desorption (TPD) to investigate the interaction between NO and the as-prepared photocatalysts. Given that photocatalysis is a room-temperature process, the adsorption of NO over the samples is intentionally set at room temperature until the equilibrium is reached. Fig. 7 shows that LFO has three distinguishable desorption peaks, with the peak around 150 °C assigned to the desorption of weakly bound NO and partly converted NO₂, the peak at 420 °C assigned to the desorption of NO, NO₂ and O₂, and the one at high temperature around 620 °C associated with the desorption of O₂ from the LFO lattice or the dissociation of strongly bound NO [52–54]. The irreversible desorption process indicates that NO are chemically adsorbed onto LaFeO₃ surface even at room temperature. For comparison, the NO desorption as a function of temperature from the LFO-STO_{0.3} composite is also presented. Clearly the composite also shows two peaks assigning to NO desorption at low and medium temperature, while the obvious distinction from the bare LFO is the strong desorption of NO at 720 °C [55]. The high temperature desorption behavior suggests that SrTiO₃ possesses stronger chemical binding force towards NO, and along with LaFeO₃ increases the chemisorption process. It is assumed that the specific chemisorption of the composite may affect the pathway of photocatalytic NO degradation, which will be explained in the next section.

3.3.3. NO photo-degradation mechanism by scavenger tests and electron spin resonance

Before proposing the reaction mechanism of photocatalytic NO oxidation, the scavenger tests and electron spin resonance (ESR) were used to determine the type of active species and their contributions. Potassium dichromate, potassium iodide and methanol were added to capture electrons, holes and •OH, respectively [42,56]. From Fig. 8a it is found out that the addition of potassium dichromate acutely suppresses the removal of NO and even results in a huge increase of NO concentration, whereas the inhibition effect imposed by potassium iodide and methanol is far less than potassium dichromate. This suggests that electrons are the most important participants for NO removal, followed by holes and •OH radicals. In particular, the sharp increase of NO concentration with using the potassium dichromate as scavenger agent could be attributed to a desorption of NO, which initially adsorbed on the LFO-STO heterojunction composite surface. After the potassium dichromate captures a photo-generated electron, the

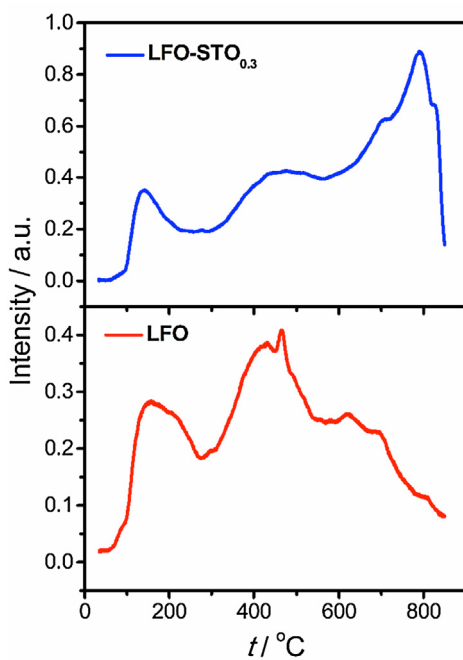


Fig. 7. TPD profiles of NO for the as-prepared pristine LaFeO_3 and $\text{LFO-STO}_{0.3}$.

Cr^{6+} reduces into the Cr^{5+} with a lone-pair electron, that induces the lone pair bond weakening effect for N–H and O–H bonds [57,58], thereby resulting in the NO desorption due to the strong competitive adsorption of the scavenger agent on the surface of the LFO-STO heterojunction composite. As the potassium dichromate with Cr^{5+} captures more photo-generated electrons and the lone-pair electron disappears, NO can be re-adsorbed on the surface of the LFO-STO heterojunction composite. Therefore, the NO concentration slowly decreased as shown in Fig. 8a. Besides, we further conducted the ESR measurement using DMPO as spin-trapping agent under visible light excitation, as presented in Fig. 8b and c. The spectra shows that both DMPO-•OH and DMPO-•O₂[−] adducts ($a_N = a_H = 1.49$ mT) with stronger signals are observed from the $\text{LFO-STO}_{0.3}$ composite than the LaFeO_3 counterpart. This further indicates that the charge transfer at the LFO-STO interfaces promoted the generation of oxygen radicals. The DMPO-•OH adduct with seven peaks (at intensity of 1:2:1:2:1:2:1) and ESR spectral parameters $g = 2.0048$, $a_N = 7.2$ G and $a_H = 4.1$ G is attributed to the formation of 5,5-dimethyl-2-ketopyrrolidino-1-oxyl (DMPOX) adduct, an oxidized derivative of DMPO [59,60], which is usually generated from DMPO oxidation by two •OH radicals, sometimes happened when super oxidative species are present, e.g., Fe^{3+} . So the ESR results confirm the generation of reactive species and their involvement in NO conversion. Since the conduction band potential of SrTiO_3 is more negative than the O_2 reduction potential (-0.33 V vs. NHE for O_2/O_2^- redox pair), the photo-transferred electrons on SrTiO_3 can reduce surface-trapped oxygen to generate •O₂[−]. However, the photo-induced holes accumulated on LaFeO_3 cannot oxidize surface-bound water or hydroxyl group into •OH (2.38 V vs NHE), due to the more negative valence band potential of LFO. Therefore, the observed DMPO-•OH signal is most likely to transform through reduction of •O₂[−] via the $\text{•O}_2^- \rightarrow \text{H}_2\text{O}_2 \rightarrow \text{•OH}$ route. This also accounts for the minor inhibition effect of methanol addition on NO removal in Fig. 8a.

On the basis of above results and analyses, we propose the NO oxidation pathway on the surface of LFO-STO composite photocatalyst as follows:

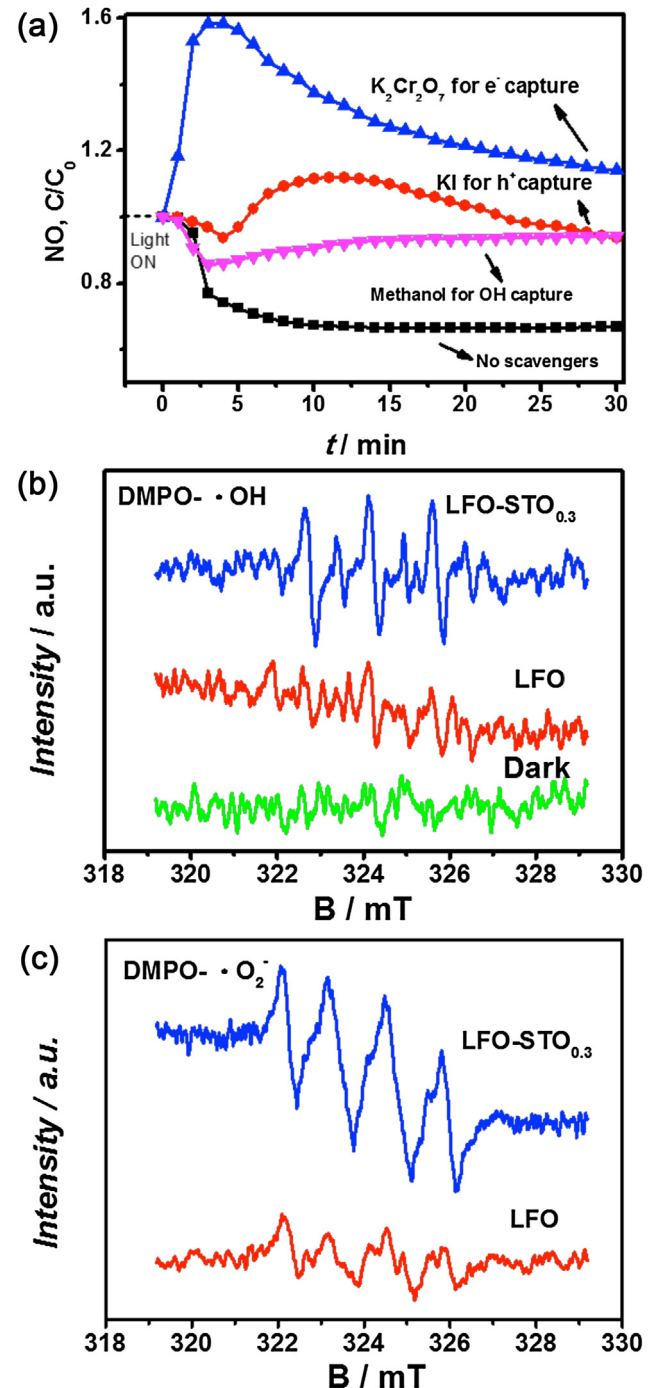


Fig. 8. (a) NO removal profile under visible light irradiation with the addition of potassium dichromate, potassium iodide and methanol as electrons, holes and •OH scavengers, respectively; (b) ESR signals of DMPO-•OH spin adduct in ethanol dispersion of the pristine LFO and $\text{LFO-STO}_{0.3}$ composite in the dark and under illumination for 3 min ($\lambda \geq 420$ nm); (c) DMPO-•O₂[−] spin adduct in ethanol dispersion of the pristine LFO and $\text{LFO-STO}_{0.3}$ composite under illumination for 3 min ($\lambda \geq 420$ nm).





LaFeO₃ is excited by visible light ($\lambda \geq 420$ nm) to produce photo-electrons which are then transferred to the conduction band of SrTiO₃, leaving behind holes on its valence band (Eqs. (1)–(2)). Since the valence band potential of LFO is 1.55 V vs. NHE which cannot oxidize OH[−] into •OH, and also because of the specific chemisorption of LFO towards NO, the photo-induced holes can directly transfer and oxidize NO into NO₂ (NO₂/NO, 1.03 V vs. NHE), HNO₂ (HNO₂/NO, 0.99 V vs. NHE) or HNO₃ (HNO₃/NO, 0.94 V vs. NHE) [37]. The ion chromatography data shows that the primary oxidation product remained on the surface of LFO-STO_{0.3} composite is NO₃[−] (4.17 µg/mL) instead of NO₂[−] (0.242 µg/mL), so the NO → HNO₃ route is more favorable (Eq. (3)). In the meantime, the electrons on conduction band of STO are captured by O₂ to produce •O₂[−] and •OH radicals (Eqs. (4)–(6)), which finally leads to the complete oxidation of NO_x into nitrates (Eqs. (7)–(9)).

4. Conclusions

In summary, we employed a two-step solution method to fabricate perovskite LaFeO₃–SrTiO₃ composites, which exhibit significantly enhanced photocatalytic activity towards NO removal (at ppb level) under visible light excitation. The synergistically improved activity is due to broad visible light harvest, enlarged surface area, and most importantly, the depressed surface charge recombination originating from the perfectly matched LaFeO₃–SrTiO₃ interface and facile charge transfer along the staggered band alignment. The ESR spectra, scavenger tests and DFT calculations results indicate that superoxide radicals (•O₂[−]) are more important reactive oxygen species for NO photo-degradation. Besides, due to the specific chemisorption of perovskite towards NO, direct h⁺ transfer is also an important route for NO oxidation. This study suggests that except being good thermal catalyst for NO_x reduction from stationary sources, the perovskite nanomaterials could potentially serve as excellent photocatalysts for NO_x oxidation from the surrounding polluted air.

Conflict of interest

The authors declare no competing financial interest.

Acknowledgements

This research was financially supported by the National Key Research and Development Program of China (2016YFA0203000), the National Science Foundation of China (41401567, 41573138), the Key Project of International Cooperation of the Chinese Academy of Sciences (GJHZ1543), and China Postdoctoral Science Foundation (Y590071524). Yu Huang is also supported by the “Hundred Talent Program” of the Chinese Academy of Sciences.

Appendix A. Supplementary data

Supplementary data associated with this article can be found, in the online version, at <http://dx.doi.org/10.1016/j.apcatb.2016.11.052>.

References

- [1] J. Lasek, Y.H. Yu, J.C.S. Wu, *J. Photochem. Photobiol. C* 14 (2013) 29–52.
- [2] P. Granger, V.I. Parvulescu, *Chem. Rev.* 111 (2011) 3155–3207.
- [3] R.-J. Huang, Y. Zhang, C. Bozzetti, K.-F. Ho, J.-J. Cao, Y. Han, K.R. Daellenbach, J.G. Slowik, S.M. Platt, F. Canonaco, P. Zotter, R. Wolf, S.M. Pieber, E.A. Bruns, M. Crippa, G. Ciarelli, A. Piazzalunga, M. Schwikowski, G. Abbaszade, J. Schnelle-Kreis, R. Zimmermann, Z. An, S. Szidat, U. Baltensperger, I.E. Haddad, A.S.H. Prevot, *Nature* 514 (2014) 218–222.
- [4] H. Wang, S. Gao, F. Yu, Y. Liu, X. Weng, Z. Wu, *J. Phys. Chem. C* 119 (2015) 15077–15084.
- [5] K. Fujiwara, U. Müller, S.E. Pratsinis, *ACS Catal.* 6 (2016) 1887–1893.
- [6] M. Signoretto, E. Ghedini, V. Trevisan, C.L. Bianchi, M. Ongaro, G. Cruciani, *Appl. Catal. B* 95 (2010) 130–136.
- [7] A. Gandolfo, V. Bartolomei, E.G. Alvarez, S. Tili, S. Gligorovski, J. Kleffmann, H. Wortham, *Appl. Catal. B* 166–167 (2014) 84–90.
- [8] M. Gallus, V. Akylas, F. Barmpas, A. Beeldens, E. Boonen, A. Boréave, M. Cazaunau, H. Chen, V. Daële, J.F. Doussin, *Build. Environ.* 84 (2015) 125–133.
- [9] M.M. Ballari, H.J.H. Brouwers, J. Hazard. Mater. 254–255 (2013) 406–414.
- [10] T. Sano, N. Negishi, K. Koike, K. Takeuchi, S. Matsuzawa, *J. Mater. Chem.* 14 (2004) 380–384.
- [11] F. Dong, Q. Li, Y. Sun, W.K. Ho, *ACS Catal.* 4 (2014) 4341–4350.
- [12] W. Ho, Z. Zhang, W. Lin, S. Huang, X. Zhang, X. Wang, Y. Huang, *ACS Appl. Mater. Interfaces* 7 (2015) 5497–5505.
- [13] J. Lyu, L. Zhu, C. Burda, *Catal. Today* 225 (2014) 24–33.
- [14] M.A. Gómez-García, V. Pitchon, A. Kiennemann, *Environ. Int.* 31 (2005) 445–467.
- [15] J. Zhu, H. Li, L. Zhong, P. Xiao, X. Xu, X. Yang, Z. Zhao, J. Li, *ACS Catal.* 4 (2014) 2917–2940.
- [16] S. Thirumalairajan, K. Girija, I. Ganesh, D. Mangalaraj, C. Viswanathan, A. Balamurugan, N. Ponpandian, *Chem. Eng. J.* 209 (2012) 420–428.
- [17] K.M. Parida, K.H. Reddy, S. Martha, D.P. Das, N. Biswal, *Int. J. Hydrogen Energy* 35 (2010) 12161–12168.
- [18] M.A. Peña, J.L.G. Fierro, *Chem. Rev.* 101 (2001) 1981–2018.
- [19] Q. Wu, G. Mul, R.V.D. Krol, *Energy Environ. Sci.* 4 (2011) 2140–2144.
- [20] V. Celorrio, K. Bradley, O.J. Weber, S.R. Hall, D.J. Fermín, *ChemElectroChem* 1 (2014) 1667–1671.
- [21] K.G. UpulWijayanta, S. Saremi-Yarahmadi, L.M. Peter, *Phys. Chem. Chem. Phys.* 13 (2011) 5264–5270.
- [22] J. Liu, S. Yang, W. Wu, Q. Tian, S. Cui, Z. Dai, F. Ren, X. Xiao, C. Jiang, *ACS Sustain. Chem. Eng.* 3 (2015) 2975–2984.
- [23] A. Yamamoto, Y. Mizuno, K. Teramura, S. Hosokawa, T. Tanaka, *Appl. Catal. B* 180 (2016) 283–290.
- [24] Y. Huang, Y. Gao, Q. Zhang, J.-J. Cao, R.-J. Huang, W. Ho, S.C. Lee, *Appl. Catal. A* 515 (2016) 170–178.
- [25] Q. Zhang, Y. Huang, L.F. Xu, J.J. Cao, W. Ho, S.C. Lee, *ACS Appl. Mater. Interfaces* 8 (2016) 4165–4174.
- [26] H. Fan, T. Jiang, H. Li, D. Wang, L. Wang, J. Zhai, D. He, P. Wang, T. Xie, *J. Phys. Chem. C* 116 (2012) 2425–2430.
- [27] M.D. Segall, P.J.D. Lindan, M.G. Probert, C.J. Pickard, P.J. Hasnip, S.J. Clark, M.C. Payne, *J. Phys.: Condens. Matter* 14 (2002) 2717–2744.
- [28] W. Yang, R.G. Parr, Oxford University Press (1989).
- [29] J.P. Perdew, K. Burke, M. Ernzerhof, *Phys. Rev. Lett.* 77 (1996) 3865–3868.
- [30] S.L. Dudarev, G.A. Botton, S.Y. Savrasov, C.J. Humphreys, A.P. Sutton, *Phys. Rev. B: Condens. Matter Mater. Phys.* 57 (1998) 1505–1509.
- [31] R.S. Mulliken, *J. Chem. Phys.* 23 (1955) 1833–1840.
- [32] D. Sharma, S. Upadhyay, V.R. Satsangi, R. Shrivastav, U.V. Waghmare, S. Dass, *J. Phys. Chem. C* 118 (2014) 25320–25329.
- [33] Z.X. Wei, Y.Q. Xu, H.Y. Liu, C. Hu, J. Hazard. Mater. 165 (2009) 1056–1061.
- [34] S. Thirumalairajan, K. Girija, N.Y. Hebbalcar, D. Mangalaraj, C. Viswanathan, N. Ponpandian, *RSC Adv.* 3 (2013) 7549–7561.
- [35] J. Luo, P.A. Maggard, *Adv. Mater.* 18 (2006) 514–517.
- [36] M. Niu, F. Huang, L. Cui, P. Huang, Y. Yu, Y. Wang, *ACS Nano* 4 (2010) 681–688.
- [37] J.I. Langford, A.J.C. Wilson, *J. Appl. Crystallogr.* 11 (1978) 102–113.
- [38] C. Zhang, C. Wang, W. Zhan, Y. Guo, Y. Guo, G. Lu, A. Baylet, A. Giroir-Fendler, *Appl. Catal. B* 129 (2013) 509–516.
- [39] K. Peng, L. Fu, H. Yang, J. Ouyang, *Sci. Rep.* 6 (2016) 19723.
- [40] W. Xun, P. Hug, R. Fige, M. Trottmann, A. Weidenkaff, D. Ferri, *Appl. Catal. B* 94 (2010) 27–37.
- [41] R. Abazari, S. Sanati, L.A. Saghatforoush, *Mater. Sci. Semicond. Process.* 25 (2014) 301–306.
- [42] S. Ge, L. Zhang, *Environ. Sci. Technol.* 45 (2011) 3027–3033.
- [43] Q. Zhang, V. Celorrio, K. Bradley, F. Eisner, D. Cherns, W. Yan, D.J. Fermín, *J. Phys. Chem. C* 118 (2014) 18207–18213.
- [44] X. Chang, T. Wang, P. Zhang, J. Zhang, A. Li, J. Gong, *J. Am. Chem. Soc.* 137 (2015) 8356–8359.
- [45] L. Kavan, M. Grätzel, S.E. Gilbert, C. Klemenz, H.J. Scheel, *J. Am. Chem. Soc.* 118 (1996) 6716–6723.
- [46] N. Baram, Y. Ein-Eli, *J. Phys. Chem. C* 114 (2010) 9781–9790.
- [47] Z. Min, B. Jian, X. Yang, Z. Jiajia, X. Junfeng, G. Meili, W. Chengliang, W. Liaoqiong, L. Yong, X. Yi, *ACS Nano* 8 (2014) 7088–7098.
- [48] L.G. Arriaga, A.M. Fernández, *Int. J. Hydrogen Energy* 27 (2002) 27–31.
- [49] P. Wang, T.F. Xie, H.Y. Li, L. Peng, Y. Zhang, T.S. Wu, S. Pang, Y.F. Zhao, D.J. Wang, *Chem. Eur. J.* 15 (2009) 4366–4372.
- [50] L. Jing, Y. Qu, H. Su, C. Yao, H. Fu, *J. Phys. Chem. C* 115 (2011) 12375–12380.
- [51] J. Wang, J. Zhao, F.E. Osterloh, *Energy. Environ. Sci.* 8 (2015) 2970–2976.
- [52] Z. Zhen, X. Yanga, W. Yue, *Appl. Catal. B* 8 (1996) 281–297.
- [53] E.N. Armstrong, T. Striker, V. Ramaswamy, J.A. Ruud, E.D. Wachsman, *Sens. Actuators B* 158 (2011) 159–170.
- [54] T. Ishihara, M. Ando, K. Sada, K. Takiishi, H. Nishiguchi, Y. Takita, K. Yamada, *J. Catal.* 220 (2003) 104–114.

[55] B. Białobok, J. Trawczyński, T. Rzadki, W. Miśta, M. Zawadzki, *Catal. Today* 119 (2007) 278–285.

[56] X. Ding, K. Zhao, L. Zhang, *Environ. Sci. Technol.* 48 (2014) 5823–5831.

[57] D. Lauvergnat, P.C. Hiberty, *J. Mol. Struct.: Theochem.* 338 (1995) 283–291.

[58] D. Lauvergnat, P. Maitre, P.C. Hiberty, F. Volatron, *J. Phys. Chem.* 100 (1996) 6463–6468.

[59] Y. Huang, W. Wang, Q. Zhang, J.J. Cao, R.J. Huang, W. Ho, S.C. Lee, *Sci. Rep.* 6 (2016) 23435.

[60] P.J. Thornalley, R.J. Trotta, A. Stern, *Biochimica Et Biophysica Acta* 759 (1983) 16–22.